Wavefront detection performance analysis of plenoptic sensor*

JIANG Tao[1,2,3], ZHANG Jinghui[1,3], WANG Haitao[1,3], QIAO Chunhong[1,3], and FAN Chengyu[1,3]**

1. Key Laboratory of Atmospheric Optics, Anhui Institute of Optics and Fine Mechanics, Hefei Institutes of Physical Science, Chinese Academy of Sciences, Hefei 230031, China

2. University of Science and Technology of China, Hefei 230026, China

3. Advanced Laser Technology Laboratory of Anhui Province, Hefei 230037, China

(Received 17 February 2023; Revised 31 March 2023)

A numerical simulation model of plenoptic sensor aberration wavefront detection is established to simulate and analyze the detection performance of plenoptic sensor aberration wavefront for different turbulence intensities. The results show that the plenoptic sensor can achieve better distortion wavefront detection, and its wavefront detection accuracy improves with turbulence intensity. The unique optical structure design of the plenoptic sensor makes it more suitable for aberration wavefront detection in strong turbulent conditions. The wavefront detection performance of the plenoptic sensor is not only related to its wavefront reconstruction algorithm but also closely related to its structural parameter settings. The influence of structural parameters on the wavefront detection accuracy of plenoptic sensors under different turbulence intensities is simulated and analyzed. The variation law of wavefront detection accuracy and structural parameters under different turbulence intensities is summarized to provide a reference for the structural design and parameter optimization of plenoptic sensors.

Document code: A **Article ID:** 1673-1905(2023)09-0526-6

DOI https://doi.org/10.1007/s11801-023-3026-9

With the proposal and development of light field theory, light field imaging technology inherits the theory and design ideas of the traditional imaging system and realizes novel imaging effects through innovative imaging models and improving hardware design[1-3]. The imaging property of optical field imaging techniques to obtain four-dimensional optical field information has led to a wide range of applications in super-resolution imaging[4,5], optical field compression[6,7], and optical field depth estimation[8,9].

Adaptive optics is an effective technical means to correct or compensate for the distortion wavefront and has been widely used in laser communication, beam purification, astronomical observation, and other fields[10-12]. The Wavefront sensor is an integral part of the adaptive optics system, which is used for real-time detection of distortion wavefront information. The commonly used wavefront sensor includes the Shake-Hartman wavefront sensor[13], curvature wavefront sensor[14], etc. With the development of wavefront detection technology, wavefront sensors based on light field structure are gradually applied to wavefront detection. In the light field images obtained by light field structure wavefront sensors, the position and angle of the light field information can be seen, and the wavefront information of the incident beam can be reconstructed according to the solution of the light field information.

CLARE et al[15] built a prototype wavefront sensor for optical field cameras by adding an objective lens to the Hartmann wavefront sensor and placing a microlens array at the focal plane position behind the objective lens. They realized the measurement of aberrated wavefronts. RODRIGUEZ-RAMOS et al[16] patented an optical field camera used as a wavefront sensor-CAFADIS camera. The CAFADIS camera uses Fourier slicing technique for aberration wavefront reconstruction and parallel computing using graphics processing unit (GPU) and field programmable gate array (FPGA) to speed up wavefront detection and wavefront reconstruction to meet the adaptive optics demand for real-time correction. WU et al[17] improved the structural basis of the optical field camera, and the modified optical field structured wavefront sensor was called a plenoptic sensor. The modified plenoptic sensor has the same aberration wavefront detection capability as the wavefront sensor of the optical field camera.

* This work has been supported by the National Natural Science Foundation of China (No.61605223), the Strategic Priority Research Program of Chinese Academy of Sciences (No.614A010717), and the Director Fund of Advanced Laser Technology Laboratory of Anhui Province (No.AHL2021ZR06).

** E-mail: jhzhang@aiofm.ac.cn

Research on the wavefront detection neighborhood of plenoptic sensors has mainly focused on the direction of aberrated wavefront reconstruction[18], phase discontinuity detection[19], and wavefront reconstruction algorithm improvement[20,21]. Plenoptic sensor wavefront detection performance at different turbulence intensities and the effect of its structural parameters on wavefront detection performance have not been studied much.

In this paper, a numerical simulation model of plenoptic sensor aberration wavefront detection is established to simulate and study the plenoptic sensor's aberration wavefront detection performance under different turbulence intensities. The wavefront detection performance of the plenoptic sensor is not only related to the wavefront reconstruction algorithm but also closely related to its structural parameter setting. In order to further improve the wavefront detection accuracy of the plenoptic sensor, the influence law of plenoptic sensor structure parameters on wavefront detection performance under different turbulence intensities is analyzed, which provides a reference for the structure design and parameter optimization of the plenoptic sensor.

The numerical simulation model of plenoptic sensor distortion wavefront detection mainly consists of three parts, beam module, distortion wavefront module, and plenoptic sensor wavefront detection module. The collimated incident beam passes through the distorted wavefront module generated by the turbulent phase screen and changes into the distorted beam affected by the turbulence. The plenoptic sensor receives the distortion beam, and the beam is transformed. The distortion wavefront information of the distortion beam can be calculated according to the light field image collected by the plenoptic sensor. A numerical simulation model of the distorted wavefront detection of the plenoptic sensor is shown in Fig.1.

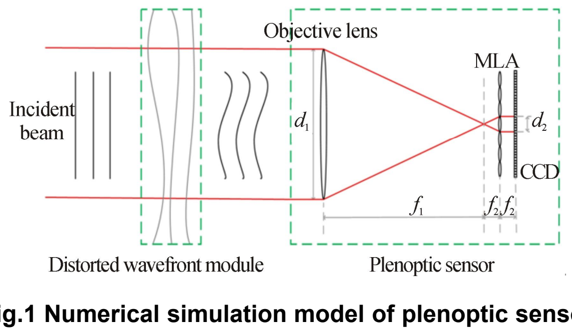

Fig.1 Numerical simulation model of plenoptic sensor distortion wavefront detection

The plenoptic sensor consists of an objective lens, a microlens array, and an image sensor. The microlens array's front focal plane coincides with the objective lens's rear focal plane, and the image sensor is located at the rear focal plane of the microlens array. The unique optical structure design of the plenoptic sensor enables the light field image to record the direction and position information of the light simultaneously, and the distortion wavefront information of the incident beam can be reconstructed by solving the light field image information.

To ensure that the incident beam of the plenoptic sensor is imaged separately by the microlens without overlapping with the adjacent microlens imaging, the parameters of the objective lens and microlens array shall meet the comparison expression[17] as

$$\frac{d_2}{f_2} \geq \frac{d_1}{f_1}, \tag{1}$$

where d_1 is the objective diameter, f_1 is the objective focal length, d_2 is the microlens diameter, and f_2 is the microlens focal length respectively. Primary and microlenses matching numerical aperture are usually used to maximize the use of all pixels within each microlens without aliasing.

The objective lens of the plenoptic sensor performs the Fourier transform of the distorted beam in the incident plane. The Fourier transform exchanges the position and angle information of the incident beam, and the rear focal plane beam of the objective lens can be expressed as

$$t_2(u,v) = \frac{1}{\mathrm{j}\lambda f_1}\int_{-\infty}^{\infty}\int_{-\infty}^{\infty} t_1(x,y)\times \exp\left(-\mathrm{j}\frac{2\pi}{\lambda f_1}(xu+yv)\right)\mathrm{d}x\mathrm{d}y, \tag{2}$$

where $t_1(x, y)$ is the amplitude of the incident beam and $t_2(u, v)$ is the amplitude at the objective's rear focal plane. The microlens array samples the transformed beam, the light of the lower angular spectrum is sampled by the microlens unit close to the center of the microlens array, and the light of the higher angular spectrum is sampled by the microlens unit away from the center.

After sampling the microlens, a second Fourier transform of the beam is applied to decoding the sub-Fourier spectrum in the area of each microlens unit into the air-space form, and the image sensor collects the light field image at the focal plane after the microlens array. The plenoptic sensor reverse scales the amplitude of the incident beam in the light field image and maps the wavefront information to the microlens cell index. The cumulative intensity of each sub-aperture image can express the light field intensity of the light field image:

$$I_i(s,t) = \sum_{k=1}^{N} I_i(s',t';M,N,k), \tag{3}$$

where (s, t) is the imaging plane coordinates, (s', t') is the local coordinates of the sub-aperture image, (M, N) is the microlens cell index, and k is the wavenumber.

The whole light field image is divided into a series of sub-aperture images represented by local coordinates. Then the wavefront phase gradient is solved according to the light intensity information of each sub-aperture image and the corresponding cell index. Wavefront phase gradient g^x and g^y can be expressed as

$$g^x : \sum_M \sum_N I_i(s', t'; M, N, k) \to \frac{\sum_M \sum_N \frac{Md_2}{f_1} I_i^n\left(-\frac{f_2}{f_1}x, -\frac{f_2}{f_1}y; M, N, k\right)}{\sum_M \sum_N I_i^n\left(-\frac{f_2}{f_1}x, -\frac{f_2}{f_1}y; M, N, k\right)}, \quad (4)$$

$$g^y : \sum_M \sum_N I_i(s', t'; M, N, k) \to \frac{\sum_M \sum_N \frac{Nd_2}{f_1} I_i^n\left(-\frac{f_2}{f_1}x, -\frac{f_2}{f_1}y; M, N, k\right)}{\sum_M \sum_N I_i^n\left(-\frac{f_2}{f_1}x, -\frac{f_2}{f_1}y; M, N, k\right)}. \quad (5)$$

The wavefront information of the incident beam can be reconstructed according to the wavefront phase gradient calculated from Eq.(4) and Eq.(5).

In the simulation model, the Fourier transform and subharmonic compensation methods proposed by SCHMIDT et al[22] are used to generate a random phase screen that matches the statistical characteristics of Komolgrvo to simulate atmospherically distorted wavefronts. For the Kolmogorov turbulence spectrum model, the Kolmogorov refractive-index power spectral density is computed by[22]

$$\Phi_n^K(\kappa) = 0.033 C_n^2 \kappa^{-11/3}, \quad (6)$$

where C_n^2 is known as the refractive-index structure parameter, $\kappa = 2\pi\left(f_x\hat{\mathbf{i}} + f_y\hat{\mathbf{j}}\right)$ is angular spatial frequency in rad/m. Typically, D/r_0 denotes the turbulence intensity, where r_0 is the atmospheric coherence length, and D is the optical system aperture. When the value of D/r_0 is more significant, the stronger the turbulence intensity is and the greater the effect on the atmospheric transmission of the laser.

In the simulation model, the incident beam is the wavelength of a 632.8 nm collimated beam. The specific parameters of the simulation model are shown in Tab.1.

Tab.1 System parameters of the simulation model

Parameter	Value
Beam wavelength (nm)	632.8
Objective diameter (mm)	30
Objective focal F-number	100
Microlens aperture (μm)	500
Microlens F-number	100
CCD pixel size (μm)	7

To visually evaluate the distorted wavefront detection performance of the plenoptic sensor, the residual wavefront root means square (*RMS*) value and relative *RMS* value ε_{RMS} after wavefront reconstruction were used as evaluation indexes. The *RMS* of the residual wavefront is defined as

$$RMS = \sqrt{\mathrm{var}\{W_c - W_i\}}, \quad (7)$$

where W_c is the reconstruction wavefront by the plenoptic sensor, W_i is the initial input wavefront, and var represents the solved mathematical variance. The larger the wavefront residual value *RMS*, the lower the wavefront detection accuracy of the plenoptic sensor.

The relative *RMS* value ε_{RMS} is defined as the ratio of the root means the fair value of the residual wavefront and the root mean square value of the initial distortion wavefront, that is

$$\varepsilon_{RMS} = RMS_{res} / RMS_i, \quad (8)$$

where RMS_{res} is the *RMS* value of the residual wavefront, and RMS_i is the *RMS* value of the initial input wavefront. The smaller the value of ε_{RMS}, the higher the wavefront detection accuracy of the plenoptic sensor.

A set of distortion wavefronts for the turbulent intensity D/r_0=10 was randomly generated. The simulation results of the distortion wavefront detection by the plenoptic sensor are shown in Fig.2. The randomly generated distortion wavefront is shown in Fig.2(a), the reconstructed wavefront of the plenoptic sensor after light field mapping and light field reverse mapping is shown in Fig.2(b), and the distribution and amplitude of the reconstructed wavefront and the initial distortion wavefront are basically consistent. The residual wavefront distribution after the plenoptic sensor wavefront reconstruction is shown in Fig.2(c), and the value of the residual wavefront ε_{RMS} is 21.4%. According to the fitting of the initial distortion wavefront and the reconstructed wavefront, the coefficient distribution of the first 30-order Zernike is shown in Fig.2(d). The correlation coefficient of the Zernike polynomial coefficient of the two groups is 0.93, which is a good agreement. It can be seen from this example that the plenoptic sensor can complete the reconstruction of the distortion wavefront.

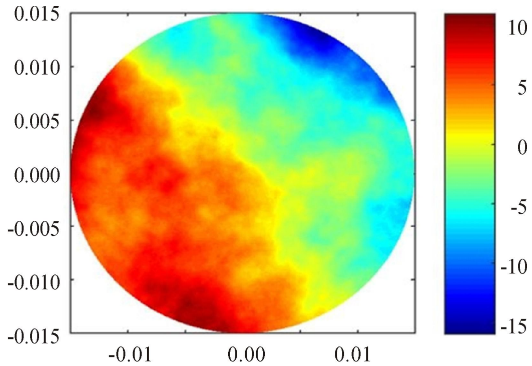

(a)

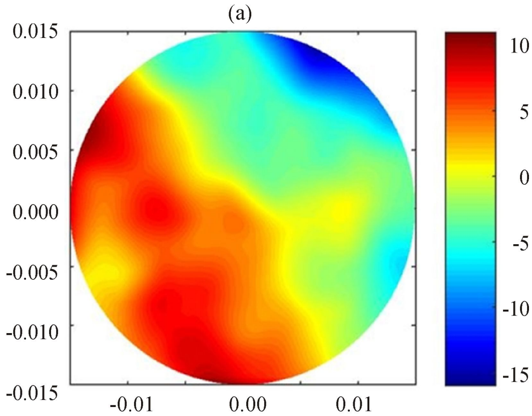

(b)

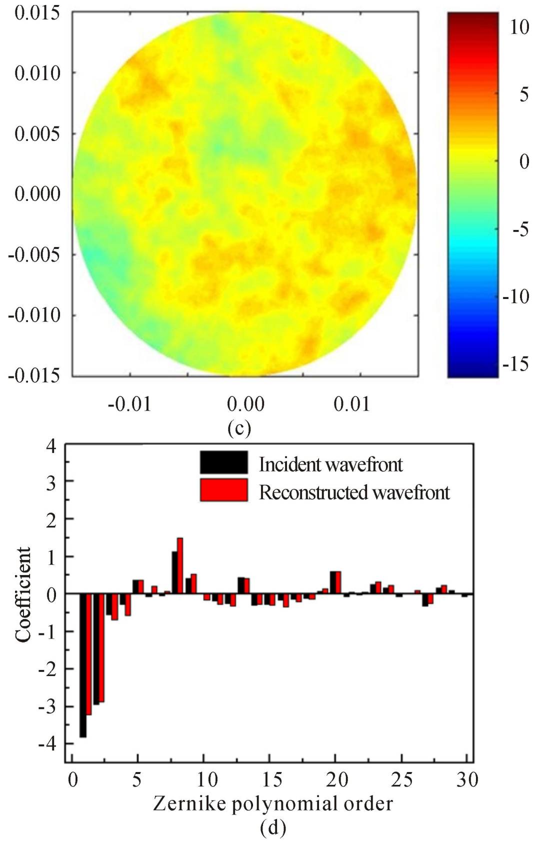

Fig.2 Aberration wavefront reconstruction results: (a) Distortion wavefront; (b) Reconstructed wavefront; (c) Residual wavefront; (d) Zernike polynomial coefficients

To fully understand the wavefront detection performance of the plenoptic sensor, simulations are performed to investigate the detection performance of the plenoptic sensor for wavefronts with different turbulence intensity distortions. Varying the magnitude of the turbulence intensity D/r_0, the ε_{RMS} values of the residual wavefront, and the correlation coefficients of the first 65-order Zernike polynomial coefficients are statistically analyzed. To eliminate the influence of the stochastic properties of atmospheric turbulence on the simulation results, the average results of 1 000 sets of random distorted wavefront detection by the plenoptic sensor at each turbulence intensity have been analyzed. The results are shown in Fig.3.

With the increase of turbulence intensity, the value of the residual wavefront gradually decreases, the correlation coefficient of the Zernike polynomial gradually increases, and the detection accuracy of detecting the distorted wavefront by the plenoptic sensor gradually increases.

When the turbulence is weak, the plenoptic sensor detects the distorted wavefront less accurately. Because the plenoptic sensor parameters set in the simulation model improve the spatial resolution of wavefront detection of the plenoptic sensor, its angular resolution decreases. Hence, the wavefront detection accuracy of the plenoptic sensor is low under weak turbulence. As the turbulence intensity increases, the distortion beams affected by turbulence are imaged by more microlensing units, thus obtaining more phase gradient sample data. The distortion wavefront reconstruction is more accurate. The unique optical structure design makes the plenoptic sensor more suitable for distortion wavefront detection under strong turbulent conditions.

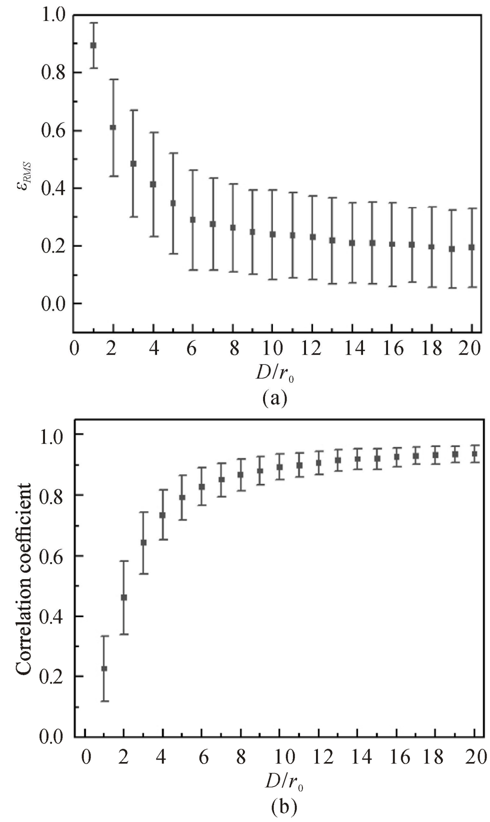

Fig.3 Wavefront detection performance of plenoptic sensor at different turbulence intensities: (a) Relative *RMS* value; (b) Correlation coefficient of Zernike polynomial coefficients

The plenoptic sensor's wavefront detection performance is related to the wavefront reconstruction algorithm and significantly related to its structural parameters design. The structural parameters of the plenoptic sensor mainly include the objective lens parameters, microlens parameters, and CCD parameters. Moreover, the optical system parameters determine the objective lens diameter, so the influence of the objective aperture is not considered.

Based on the parameters of the simulation model in Tab.1, the structural parameters of the plenoptic sensor in the simulation model are changed under the premise of satisfying Eq.(1). The *RMS* values of the residual wavefront at turbulence intensities D/r_0 of 5, 10, 15, and 20 are counted to compare and analyze the effects of structural parameters on the wavefront detection performance of the plenoptic sensor at the four turbulence intensities.

In order to eliminate the influence of the random characteristics of atmospheric turbulence on the simulation results, the average results of 1 000 sets of random aberration wavefront detections by the plenoptic sensor are taken for each turbulence intensity.

The effect of the objective focal length on the performance of the wavefront detection of the plenoptic sensor under four turbulent intensities is shown in Fig.4. It can be seen that the wavefront reconstruction accuracy of the plenoptic sensor is related to both the objective focal length and the turbulence intensity. As the focal length of the objective lens increases, the wavefront detection error of the plenoptic sensor first decreases and then gradually increases. There is an optimal objective focal length to minimize the wavefront detection error. The optimal objective focal length for the four turbulent intensities is shown in Tab.2 and decreases gradually as the turbulence intensity increases.

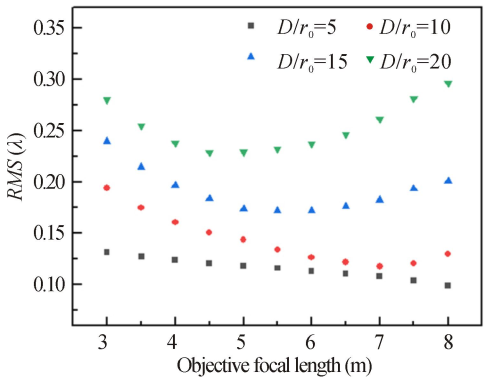

Fig.4 Effect of objective focal length on wavefront detection performance

Tab.2 Optimal objective focal lengths for different turbulence intensities

Turbulence intensity	Optimal objective focal length (m)
5	8
10	7
15	5.5
20	4.5

The influence of the microlens diameter and focal length on the wavefront detection performance of the plenoptic sensor are shown in Fig.5(a) and Fig.5(b), respectively. The wavefront detection error gradually increases as the microlens aperture increases. With the microlens diameter of 500 μm, the plenoptic sensor wavefront detection accuracy is the highest. Similarly, as the focal length of the microlens increases, the wavefront detection error first decreases gradually and then levels off. With the intensity of the turbulence increasing, the microlens focal length threshold required to smooth the wavefront detection error gradually increases. With a focal length of 50 mm, the plenoptic sensor has the highest detection accuracy.

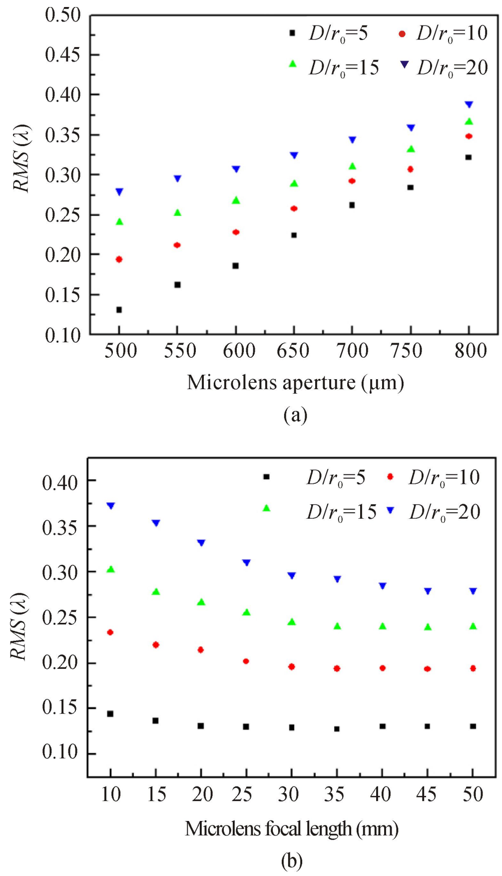

Fig.5 Effect of microlens parameters on wavefront detection performance: (a) Microlens aperture; (b) Microlens focal length

The influence of CCD pixel size on the wavefront detection performance of the plenoptic sensor is shown in Fig.6. The wavefront detection accuracy of the plenoptic sensor is related to both CCD image size and turbulence intensity. There is an optimal pixel size, so wavefront detection has the highest accuracy. The optimal pixel size tends to decrease gradually with the increase in turbulence intensity.

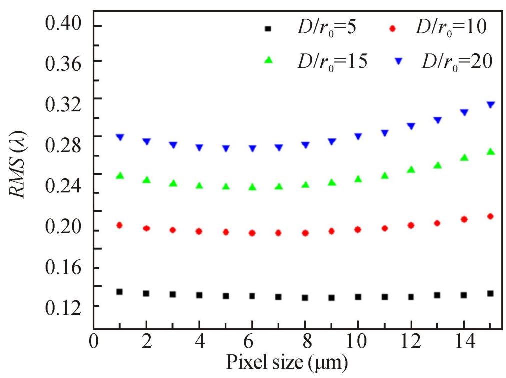

Fig.6 Effect of CCD pixel size on wavefront detection performance

A numerical simulation model of distortion wavefront detection of the plenoptic sensor is established to study the detection performance at different turbulence intensities. The results show that the plenoptic sensor can complete good distortion wavefront detection. The unique optical structure design makes it more suitable for distortion wavefront detection under strong turbulence conditions. The structure parameters of the plenoptic sensor are closely correlated to its wavefront detection performance. The simulation results show an optimal objective focal length or pixel size for different turbulence intensities, making the highest wavefront detection accuracy. As the turbulence intensity increases, the focal length of the optimal objective lens gradually decreases, and the optimal pixel size also tends to decrease gradually. Optimizing structural parameters can further improve the wavefront detection accuracy of the plenoptic sensor.

The wavefront detection performance of the plenoptic sensor and the influence law of its structural parameters on the wavefront detection accuracy are studied to provide a reference for the structural design and parameter optimization of the plenoptic sensor.

Ethics declarations

Conflicts of interest

The authors declare no conflict of interest.

References

[1] GERSHUN A. The light field[J]. Journal of mathematics and physics, 1939, 18(1-4)：51-151.

[2] ADELSON E H, WANG J Y. Single lens stereo with a plenoptic camera[J]. IEEE transactions on pattern analysis and machine intelligence, 1992, 14(2)：99-106.

[3] WU G, MASIA B, JARABO A, et al. Light field image processing：An overview[J]. IEEE journal of selected topics in signal processing, 2017, 11(7)：926-954.

[4] WANG T C, ZHU J Y, KALANTARI N K, et al. Light field video capture using a learning-based hybrid imaging system[J]. ACM transactions on graphics (TOG), 2017, 36(4)：1-13.

[5] BISHOP T E, FAVARO P. The light field camera：Extended depth of field, aliasing, and superresolution[J]. IEEE transactions on pattern analysis and machine intelligence, 2011, 34(5)：972-986.

[6] ZHAO S Y, CHEN Z B. Light field image coding via linear approximation prior[C]//Proceedings of 2017 IEEE International Conference on Image Processing, September 17-20, 2017, Beijing, China. New York：IEEE, 2017：4562-4566.

[7] HUANG X P, AN P, SHEN L Q, et al. Efficient light field images compression method based on depth estimation and optimization[J]. IEEE access, 2018, 6：48984-48993.

[8] WANG C, ZHANG J, GAO J. Anti-specular light-field depth estimation algorithm[J]. Journal of image and graphics, 2020, 25(12)：2630-2646.

[9] FAN X T, LI Y, LUO X W, et al. Depth estimation based on light field structure characteristic and multiview matching[J]. Infrared and laser engineering, 2019, 48(05)：0524001.

[10] RUI M D, LIU C, CHEN M, et al. Application of adaptive optics on the satellite laser communication ground station[J]. Opto-electronic engineering, 2018, 45(3)：49-57. (in Chinese)

[11] TAN Y, YANG P, DONG L Z, et al. Active beam cleanup of pulsed slab laser based on 59-unit adaptive optics system[J]. Scientia sinica physica, mechanica & astronomica, 2017, 47(8)：51-59. (in Chinese)

[12] DENG K R, WEI K, JIN K, et al. Research on high-contrast imaging performance of 1.8 m telescope sodium beacon adaptive optical system[J]. Infrared and laser engineering, 2020, 49(8)：281-289.

[13] WEI P, LI X Y, LUO X, et al. Influence of lack of light in partial subapertures on wavefront reconstruction for Shack-Hartmann wavefront sensor[J]. Chinese journal of lasers, 2020, 47(4)：0409002. (in Chinese)

[14] LIU R F, SHEN F. Study on algorithms for wavefront reconstruction of curvature sensor[J]. Opto-electronic engineering, 2005, 32(10)：6-9. (in Chinese)

[15] CLARE R M, LANE R G. Comparison of wavefront sensing using subdivision at the aperture and focal planes[J]. Palmerston north, 2003：187-192.

[16] RODRÍGUEZ-RAMOS M, CASTELLÁ B F, NAVA F P, et al. Wavefront and distance measurement using the CAFADIS camera[J]. Astronomical telescopes and instrumentation：synergies between ground and space, 2008, 7015：70155Q.

[17] WU C, DAVIS C C, EIJK A V, et al. Modified plenoptic camera for phase and amplitude wavefront sensing[J]. Proceedings of SPIE - the international society for optical engineering, 2013, 8874：88740I.

[18] LIU Y, QIAO C H, FENG X X, et al. Simulation of wavefront phase reconstruction by plenoptic sensor[J]. Journal of atmospheric and environmental optics, 2020, 15(2)：101-109.

[19] WU C, KO J, DAVIS C C. Using a plenoptic sensor to reconstruct vortex phase structures[J]. Optics letters, 2016, 41(14)：3169-3172.

[20] HU J, CHEN T, LIN X, et al. Improved wavefront reconstruction and correction strategy for adaptive optics system with a plenoptic sensor[J]. IEEE photonics journal, 2021, 13(4)：1-8.

[21] WANG Z, CHEN T, LIN X, et al. A local threshold checkerboard algorithm for adaptive optics system with a plenoptic sensor[J]. IEEE photonics journal, 2021, 14(1)：1-9.

[22] SCHMIDT J D. Numerical simulation of optical wave propagation with examples in MATLAB[M]. Washington：SPIE Press, 2010.